

Testing the coupling of dark radiations in light of the Hubble tension

Zhiyu Lu,^{1,2,3*} Batool Imtiaz^{1,2,3,5}, Dongdong Zhang^{1,2,3,4},
Yi-Fu Cai^{1,2,3}

¹*Department of Astronomy, School of Physical Sciences, University of Science and Technology of China, Hefei, Anhui 230026, China.

²School of Astronomy and Space Science, University of Science and Technology of China, Hefei, Anhui 230026, China.

³CAS Key Laboratory for Researches in Galaxies and Cosmology, University of Science and Technology of China, Hefei, Anhui 230026, China.

⁴Kavli IPMU (WPI), UTIAS, The University of Tokyo, 5-1-5 Kashiwanoha, Kashiwa, 277-8583, Chiba, Japan.

⁵Department of Computer Science, Mohammad Ali Jinnah University, Block-6, P.E.C.H.S, Karachi-75400 Sindh, Pakistan.

*Corresponding author(s). E-mail(s): zhiyulu@mail.ustc.edu.cn;
Contributing authors: batool24@mail.ustc.edu.cn; don@mail.ustc.edu.cn;
yifucai@ustc.edu.cn;

Abstract

We are studying the effects of Self-Interacting dark radiation (SI_{dr}) on the evolution of the universe. Our main focus is on the cosmic microwave background (CMB) and how SI_{dr} could potentially help resolve the Hubble tension. We are looking into different scenarios by mixing SI_{dr} with Free-Streaming dark radiation (FS_{dr}) or not to determine whether SI_{dr} can indeed contribute to solving the Hubble tension. We find that SI_{dr} alone can increase the Hubble constant (H_0) to $70.1_{-1.6}^{+1.3}$ km/s/Mpc with a value of $N_{\text{eff}} = 3.27_{-0.31}^{+0.23}$. However, including FS_{dr} disfavors the existence of SI_{dr} $\tilde{N}_{\text{si}} \approx 0.37$. Even though the Hubble constant is increased compared to the predicted value, it entails $N_{\text{eff}} = 3.52 \pm 0.25$. Finally, we implement the Fisher method for future experiments and a 7.64σ measurement of \tilde{N}_{si} will be obtained when combining data from Planck, AliCPT, and CMB-S4.

Keywords: Hubble Tension, Self-Interacting Dark Radiation, CMB

1 Introduction

The standard Λ CDM cosmological model has achieved remarkable success in describing the Universe’s evolutionary history, encompassing structure formation and elemental synthesis. Nevertheless, in the era of precision cosmology, it is crucial to assess both the theoretical and experimental self-consistency of the Λ CDM model. Despite its overall success, there are indeed hints of tensions within the observed data.

One of the most pressing challenges is the discrepancy between the universe’s expansion rate as measured by the cosmic microwave background (CMB) experiments and local (low redshift) measurements [1], commonly referred to as the Hubble tension [2–4]. The observed discrepancy in the Hubble constant (H_0) between the Planck satellite’s estimation of $67.27 \pm 0.60 \text{ km s}^{-1} \text{ Mpc}^{-1}$ [5] and the measurement of $73.24 \pm 1.74 \text{ km s}^{-1} \text{ Mpc}^{-1}$ [1] by the SH0ES collaboration amounts to more than 3σ [6] (3 to 5 sigma tension based on different datasets). If it exists, this tension strongly indicates the presence of new physics beyond the Λ CDM model.

Establishing a theoretical framework to resolve the Hubble tension is a daunting task. From the perspective of CMB power spectrum analysis, the precise determination of the acoustic peak angular scale θ_s is crucial, as it determines both the sound horizon at decoupling r_s and the distance D_A to the CMB surface of last scattering via $\theta_s = r_s/D_A$. One class of models aims to reduce the sound horizon to alleviate the Hubble tension. For example, the early dark energy (EDE) model introduces a dark-energy-like component that becomes active around the matter-radiation equality and dilutes thereafter. Though EDE has shown promise in mitigating the tension, it has introduced new challenges, such as worsening the S_8 tension and fine-tuning problems.[7, 8]. Moreover, some efforts have been made to investigate non-standard scenarios, e.g. dark matter-radiation interaction [9–11], modified gravity paradigm [12, 13], ultra-light primordial black holes [14].

Another way to reduce sound horizon is the addition of dark radiations before recombination. This can lead to differences in the effective number of relativistic degrees of freedom N_{eff} from standard model predictions, providing a clue to new physics. N_{eff} is a key probe of the temperature evolution of the early Universe and characterizes the energy density of relativistic species, such as neutrinos. The energy contribution by photons can be determined by CMB temperature today. The remaining radiation species contributing to total radiation energy is given by

$$\rho_r(T \leq 1\text{MeV}) = \left[1 + \frac{7}{8} \left(\frac{4}{11} \right)^{\frac{4}{3}} N_{\text{eff}} \right] \rho_\gamma, \quad (1)$$

where $\rho_\gamma = (\pi/15)T_\gamma^4$ is the energy density in CMB photon with $T_\gamma = 2.725 \text{ K}$ and $N_{\text{eff}} = 3.046$ [15]¹. The Planck bestfit to Λ CDM gives $N_{\text{eff}} = 2.99 \pm 0.17$ at 68% CL

¹The most precise predication of N_{eff} up to today is 3.044 [16]

[5]. To reconcile the indirect measurements of H_0 from the CMB, Baryon Acoustic Oscillations (BAO), Type Ia Supernovae, and the direct measurements from the local distance ladder in physical theories, one may require $N_{\text{eff}} \simeq 3.95$ [17].

If we overlook the neutrino decoupling process, we can obtain $N_{\text{eff}} = 3$ by considering the conservation of entropy from $T \equiv 10$ MeV and $T \leq m_e$ [18, 19]. The deviation from the integer value of three occurring in N_{eff} is due to various factors in the early universe. For instance, neutrinos continue to interact with the primordial plasma during electron-positron annihilation, affecting their temperature. Additionally, the energy dependence of neutrino interactions allows those at the high-momentum tail to interact with SM particles, influencing the energy spectrum of the neutrino gas [20]. Thus, a high degree of confidence in the neutrino's effective degree of freedom consistent with 3.046 can provide robust evidence for the existence of SM neutrinos. On the other hand, a value higher than 3.046 could indicate the existence of additional radiations.

It has also been shown in [21] that both the damping tail and phase shift allow us to jointly constrain the amount of free-streaming relativistic particles N_{eff} , and the number of relativistic particles that are fluid-like and tightly coupled. Likewise, the analysis of large-scale structure information provides insight into the phase of the acoustic oscillations, allowing constraints on N_{eff} [22–24]. Though Λ CDM has predicted three flavors of neutrinos [25], several terrestrial neutrino experiments have found anomalies against the standard picture, which may be an indication of the existence of dark radiation [26]. Cosmological data also indicates additional radiations [27].

In fact, any physical mechanism capable of generating additional radiation will result in the same impacts on the background expansion as extra neutrinos do, leading to an increased N_{eff} value in observations. Given the numerous models that can boost N_{eff} , it's crucial to explore methods for distinguishing among them such as sterile neutrinos [28, 29], self-interacting neutrinos [30, 31] and ultra-light axion-like fields [32, 33]. If the extra radiation consists of relativistic particles like sterile neutrinos, it should exhibit behaviour similar to that of regular neutrinos in terms of perturbation theory.

Some recent work investigates the effect of changing the nature of radiation. Motivated by this, a recent study [30] proposed a framework involving self-interacting neutrinos with a non-vanishing sum of their masses. They suggest a significant increase in the value of Hubble constant $H_0 = 72.3 \pm 1.4$ km/s/Mpc, along with a lower value of the matter fluctuations, $\sigma_8 = 0.786 \pm 0.020$, while preserving the fit to the CMB damping tail. This study investigates $N_{\text{eff}} = 4.02 \pm 0.29$. Das [34] considered the neutrino coupling between flavors, and a strong interacting mode can be a better fit with CMB data. In their subsequent work, ACT data is included and supports a notable level of neutrino self-interaction, causing a delay in neutrino-free streaming until right before matter-radiation equality [35]. However, the inclusion of Planck 2018 polarization data diminishes the inclination towards a strong interaction.

In this study, our primary focus is the physics of dark radiation components. Dark radiation can be categorized as either coupled or decoupled. When decoupled, we assume it shares the same properties as neutrinos and is noted as FSdr (Free-Streaming

dark radiation for short). Going beyond the same property assumption is straightforward. For the coupled case, we focus on the self-interaction, which we refer to as SI_{dr}. These distinctions are clearly outlined in Table 1. Though neutrinos are not "dark", we include them in our FS_{dr} framework to incorporate the truly dark ones as they exhibit the same behaviour under our assumptions.

Table 1 The Categories and conventions used in this work.

Name	Neutrino	Dark Radiation	
Property	Free-Streaming	Free-Streaming	Self-Interacting
Label	N_{fs}		N_{si}
Short name	FS _{dr}		SI _{dr}

In Section 2, we present the physical impact of SI_{dr} on the power spectra. In Section 4, we constrain the parameters using the latest CMB data. Section 5 summarises the Fisher information matrix method we use in our forecasting analysis for next-generation experiments. Section 6 is dedicated to the conclusion and outlook.

2 Impact on cosmological perturbations and CMB power spectra

The self-interacting model among dark radiations intervened by a heavy mediator was developed in [36]. Those interested in details can find references therein. This section will explore the two primary factors contributed by extra radiations and SI_{dr} that can influence the universe.

Cosmological experiments, such as CMB polarization detection, provide valuable insights into the properties of radiations through two well-defined physical processes. Firstly, Thomson scattering depends on the total energy density of radiations. Before matter-radiation decoupling, over a broad span of angular scales, CMB polarization data is attenuated by the finite width of the last scattering surface in the presence of the density fluctuations with adiabatic conditions[37].

Secondly, since the time when neutrinos decouple from hot plasma, the whole universe has been transparent to them except for gravitational influence. The neutrinos will pull the photon-electron sound wave as they travel at the speed of light, while the sound speed is $1/\sqrt{3}$ times lower. Obviously, the effect of this "pull" will be stronger if there are more neutrinos or to say FS_{dr}. Thus, the amount of free-streaming particles will introduce a phase shift and diminish the amplitude of the acoustic peaks observed in the CMB [38–41]. The phase shift strongly indicates the existence of FS_{dr} [21, 23]. These effects are quantified through the parameter R_{fs} , which represents the fractional energy density contributed by the free-streaming part. It is given by

$$R_{\text{fs}} = \frac{\rho_{\text{fs}}}{\rho_r} , \quad (2)$$

where ρ_{fs} is the energy density of FS_{dr}, and ρ_r is the total energy density in radiations including photons, neutrinos and other possible dark radiations.

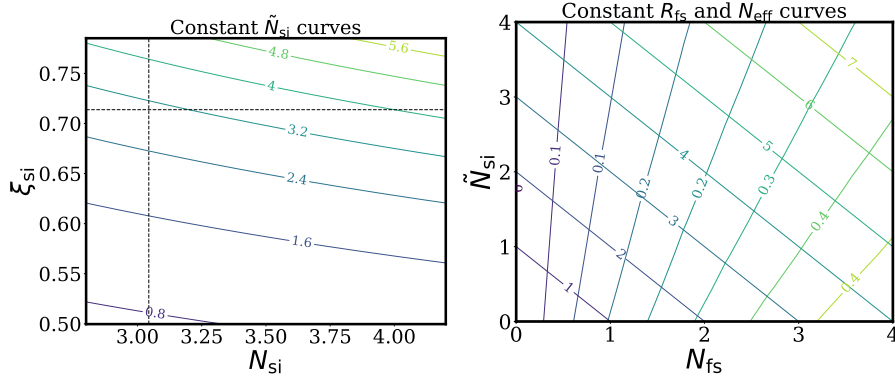


Fig. 1 **Left:** The degeneracy relation between temperature ratio ξ_{si} and flavor number N_{si} . **Right:** The degeneracy relation between FSdr number N_{fs} and SIDr \tilde{N}_{si} .

Since we don't distinguish free-streaming dark radiation with neutrinos, the following steps are direct,

$$R_{\text{fs}} = \frac{\rho_{\text{fs}}}{\rho_{\gamma} + \rho_{\text{fs}} + \rho_{\text{si}}} = \frac{\frac{7}{8} N_{\text{fs}} \xi_{\text{fs}}^4}{1 + \frac{7}{8} N_{\text{fs}} \xi_{\text{fs}}^4 + \frac{7}{8} N_{\text{si}} \xi_{\text{si}}^4} = \frac{N_{\text{fs}}}{\left(\frac{7}{8} \xi_{\text{fs}}^4\right)^{-1} + N_{\text{eff}}}, \quad (3)$$

and the effective number of species [42] is

$$N_{\text{eff}} \approx N_{\text{fs}} + N_{\text{si}} \xi_{\text{si}}^4 / \xi_{\text{fs}}^4 \equiv N_{\text{fs}} + \tilde{N}_{\text{si}}. \quad (4)$$

Here, $7/8$ stands for the statistical factor for the fermionic particles, and $\xi_{\text{si}} = T_{\text{si}}/T_{\gamma}$ is the temperature ratio of SIDr to photons. $\xi_{\text{fs}} = (4/11)^{1/3}$ is the temperature ratio between FSdr and photons. We also define the effective species number for SIDr, including the temperature effect \tilde{N}_{si} . Eq. (4) reveals the degeneracy between the temperature and the flavors of the SIDr. As depicted in Fig 1, SIDr can explain the entire dark radiation contribution when $N_{\text{si}} = 3$, $\xi_{\text{si}} = \left(\frac{4}{11}\right)^{1/3}$, and $N_{\text{fs}} = 0$, yielding $N_{\text{eff}} \approx 3.046$. However, the scenario can also be interpreted with $N_{\text{si}} \approx 4$ and $\xi_{\text{si}} \approx 0.68$. Although Eq. (4) can't capture the contribution from non-instant decoupling, the error is well within the margin of error for the current experiment capacity.

In the standard model, we have three species of FSdr (three neutrinos) and no SIDr, i.e., $R_{\text{fs}}^{\text{SM}} = 0.408$. Also, if all radiations are tightly coupled, then $R_{\text{fs}} = 0$. Thus $(N_{\text{eff}}, R_{\text{fs}})$ can be parameterized for the properties of dark radiations up to the effective species \tilde{N}_{si} . To break the degeneracy, one of the prior knowledge on $(N_{\text{si}}, \xi_{\text{si}}, G_{\text{eff}})$ is required. ²

The presence of SIDr perturbs the CMB peaks and amplitudes. In the sub-horizon region and deep in the radiation-dominated epoch, the baryon density is negligible,

²If the dark radiations are coupled, the interacting strength is a key parameter as well, making it a crucial factor.

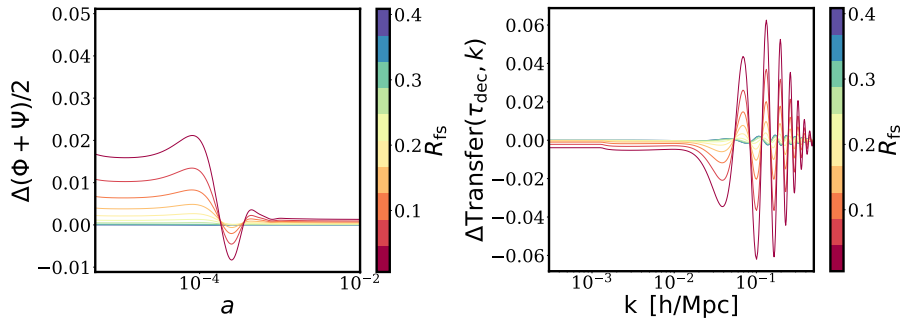


Fig. 2 **Left:** the Weyl potential evolution along scale factor at scale $k = 0.11/\text{Mpc}$; **Right:** the monopole of photon perturbation transfer function for various R_{fs} . We compare our analysis with ΛCDM by varying R_{fs} from 0 to 0.41

and the monopole of photon perturbation can be expressed as:

$$[\Theta_0 - \Phi](\tau) = [\Theta_0 - \Phi](0) \cos(kc_s\tau) - \frac{k}{\sqrt{3}} \int_0^\tau d\tau' [\Phi + \Psi](\tau') \sin[kc_s(\tau - \tau')] , \quad (5)$$

where $(\Phi + \Psi)/2$ is the Weyl potential, Θ_0 is the monopole of temperature fluctuation. The Weyl potential vanishes once the photons enter the sound horizon, leading to the radiation-driven effect of acoustic oscillations.[43, 44]. This extra source can carry a phase shift if the timing of the decay is modified, and the amplitude of the radiation-driving effect depends on the initial value of the Weyl potential

$$\Psi + \Phi = -\left(1 + \frac{5}{15 + 4R_{\text{fs}}}\right)\mathcal{R} . \quad (6)$$

Here, Φ, Ψ are the metric perturbations, and \mathcal{R} is the comoving curvature perturbation. One can observe that the decrease in fractional energy density enhances the radiation-driving effect through the shift in initial value.

The same idea can apply to the polarization multiples through the equation [39]

$$\Theta_{P,\ell}(\tau_0) \simeq \frac{5}{18} \dot{d}_\gamma(k, \tau_{\text{rec}}) \dot{\kappa}^{-1}(\tau_{\text{rec}}) \left(1 + \frac{\partial^2}{\partial(k\tau_0)^2}\right) j_\ell(k\tau_0) . \quad (7)$$

We can observe that polarization multiples are proportional to the photon temperature fluctuations, i.e., $\Theta_{P,\ell} \propto \dot{d}_\gamma$, causing them to be influenced by neutrinos in a manner similar to temperature fluctuations. Additionally, the time derivative of d_γ does not affect the phase-amplitude shift. As a result, the free-streaming radiations imprint a net phase and amplitude shift in the CMB power spectra. The shifted phase and amplitude are given by [38]

$$\phi_{\text{fs}} \approx 0.19\pi R_{\text{fs}} , \quad \Delta_{\text{fs}} \approx -0.27R_{\text{fs}} . \quad (8)$$

The presence of self-interaction between dark radiations prevents them from free-streaming and delays the decoupling time until a low redshift z_{dec} , depending on

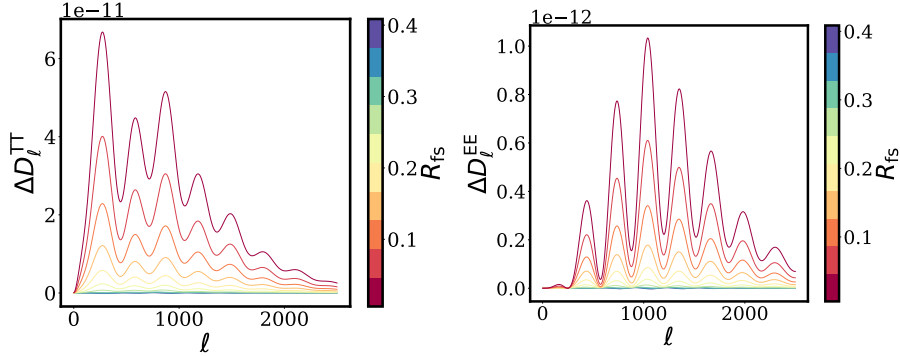


Fig. 3 Same as Fig 2, but with a displacement of the influence on CMB power spectra.

the strength of the interaction. As a result, the free-streaming neutrino fraction R_{fs} decreases relative to ΛCDM . The amplitude of the SIdr scenario in the CMB temperature power spectrum is higher compared with ΛCDM , and the peaks are also shifted to higher ℓ [38]. These self-interacting dark radiations can be described by the following Boltzmann equation in the Newtonian gauge [45–47]

$$\begin{aligned}
 \dot{\delta}_{\text{si}} + \frac{4}{3}\theta_{\text{si}} - 4\dot{\Phi} &= 0, \\
 \dot{\theta}_{\text{si}} + \frac{1}{2}k^2(F_{\text{si},2} - \frac{1}{2}\delta_{\text{si}} - 2\Phi) &= 0, \\
 \dot{F}_{\text{si},\ell} + \frac{k}{2\ell+1}(\ell+1)F_{\text{si},\ell+1} - \ell F_{\text{si},\ell-1} &= \alpha_\ell \dot{\tau}_{\text{si}} F_{\text{si},\ell}, \quad \ell \geq 2.
 \end{aligned}
 \tag{9}$$

Here, $F_{\text{si},\ell}$ is SIdr’s perturbation expanded in multiple space, $F_{\text{si},0} \equiv \delta_{\text{si}}$ and $F_{\text{si},1} \equiv \frac{4}{3k}\theta_{\text{si}}$. In the above set of equations, α_ℓ are ℓ -dependent $\mathcal{O}(1)$ angular coefficients that depend on the nature of the interacting model. Due to energy and momentum conservation, $\alpha_\ell = 0$ for $\ell = 0, 1$ while, for $\ell \geq 2$, $\alpha_\ell \approx \mathcal{O}(1)$. The subsequent opacity from dark radiation self-scattering is $\dot{\tau}_{\text{si}} \propto G_{\text{eff}}^2 T_{\text{si}}^5$, determined by the interacting strength and temperature of SIdr. During a frequently interacting period, the high moments are suppressed, and these equations then behave like a fluid. When $\dot{\tau}_{\text{si}} \rightarrow 0$, this causes Eq. (9) to mimic free streaming radiations. The transition time is determined by G_{eff} . We use the publicly available modified CLASS [48] code CLASS_SInu³ to solve above set of equations.

In Fig 3, we illustrate the evolution of the perturbation effects of net monopole, the Weyl potential and CMB TT and EE power spectra by keeping $N_{\text{eff}} = 3.046$ fixed and varying the free-streaming fraction R_{fs} from 0 to 0.408. The left panel displays the variation in the net monopole of the photon perturbation as a function of R_{fs} . In comparison to the ΛCDM scenario, the presence of SIdr exhibits a higher amplitude of acoustic oscillations, and the peaks are shifted towards smaller scales. The middle panel demonstrates that the Weyl potentials have a larger initial value in scenarios with smaller R_{fs} . Consequently, the radiation’s driving effect is intensified, leading to a delay in their decay and a phase and amplitude shift in the photon transfer function.

³https://github.com/anirbandas89/CLASS_SInu

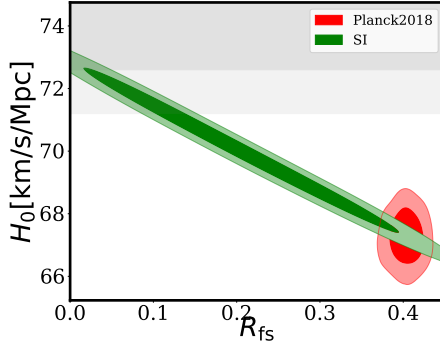


Fig. 4 The expected Hubble constant distribution in the SI scenario neglecting the parameter degeneracy. This distribution is based on the Planck measurement with possible mixing of FSdr and SI to achieve $N_{\text{eff}} \sim 3.044$. The grey shadow indicates the 1σ region allowed by SHOES.

The resulted changes in the CMB TT and EE spectra are depicted in the right panel. We observe amplified amplitudes of the power spectra and a shift of the peak positions towards larger ℓ values as R_{fs} decreases. These effects reach their maximum as R_{fs} approaches 0.

3 Cosmological probe: The Hubble tension

As explained in Sec 2, even when N_{eff} is fixed, one can manipulate the phases and amplitudes of the CMB spectra by tuning the parameter R_{fs} . This manipulation creates room for a larger Hubble constant.

The power of the SI scenario becomes apparent when considering the observed peak of the CMB multipoles ℓ_{peak} with corresponding wave numbers k_{peak} , which can be determined using the approximation equation [11]:

$$\ell_{\text{peak}} = k_{\text{peak}} D_A \approx (m\pi - \phi) \frac{D_A}{r_s}, \quad (10)$$

where $m \geq 1$ is an integer number referring to the index of the peak; ϕ is the phase, as discussed in Eq. (8); r_s is the radius of the sound horizon. Additionally, D_A is the comoving angular diameter distance to the redshift of recombination z_{rs}

$$D_A = \frac{1}{H_0} \int_0^{z_{\text{rs}}} \frac{dz}{[\rho(z)/\rho_0]^{1/2}}. \quad (11)$$

$\rho(z)$ corresponds to the energy density of the universe at redshift z , while ρ_0 stands for present-day value. We can assert that H_0 is directly related to the function of phase suppressed by the sound horizon and influenced by late-time physics involved in the integration process:

$$H_0 = \frac{m\pi - \phi}{\ell_{\text{peak}} r_s / \int_0^{z_{\text{rs}}} dz (\rho(z)/\rho_0)^{-1/2}}. \quad (12)$$

If SI_{dr} exists when N_{eff} is fixed, according to Eq. 8, there is $\phi^{\text{SI}} < \phi^{\Lambda\text{CDM}}$. As a result, the numerator of Eq. (12) becomes smaller without introducing new energy components such as early dark energy or additional relativistic degrees of freedom. This naturally requires a larger H_0 while keeping the observed ℓ_{peak} fixed.

The Hubble constant proposed by SI_{dr} model compared with ΛCDM model is

$$\frac{H_0^{\text{SI}}}{H_0^{\Lambda\text{CDM}}} = \frac{\pi - 0.19\pi R_{\text{fs}}^{\text{SI}}}{\pi - 0.19\pi R_{\text{fs}}^{\Lambda\text{CDM}}} . \quad (13)$$

We take $H_0^{\Lambda\text{CDM}}$ and N_{eff} as independent Gaussian variables from Planck best-fit $H_0 = 67.27 \pm 0.60 \text{ km/s/Mpc}$ and $N_{\text{eff}} = 2.99 \pm 0.17$. Since a lower value of R_{fs} will induce a higher H_0 , we don't consider cases $R_{\text{fs}} > 0.41$. Assuming $R_{\text{fs}}^{\text{SI}}$ has a uniform distribution between 0 to 0.41 gives us the distribution of H_0 in view of self-interacting radiations, as shown in Fig 4. Once R_{fs} is less than 0.1, the CMB deduced H_0 will be within the 2σ regime of the SH0ES prediction.

Note that Eq. 12 is approximately valid since we neglect the complicated influence of SI_{dr} on the denominator part. Eq. 13 is only used for illustrative purposes, as it couldn't capture the degeneracy between SI_{dr} and cosmological parameters.

4 Methodology

In this work, we consider the contribution of SI_{dr} to N_{eff} by introducing the temperature ratio ξ_{si} between SI_{dr} and photons as a free parameter. Since it is the value N_{eff} that directly affects observations, the combination of ξ_{si} and the flavor of the SI_{dr} N_{si} introduces degeneracy, as discussed in Section 2, we therefore work with $N_{\text{si}} = 4$ throughout this paper, inspired by the flavors of active and sterile neutrinos. N_{si} shouldn't be confused with \tilde{N}_{si} , the latter is the effective species number considering the temperature difference. N_{si} can be set arbitrarily, as the data can only constrain the combination of N_{si} and ξ_{si} . Another free parameter in our analysis is the effective self-interacting strength $\log_{10}[G_{\text{eff}}/\text{MeV}^{-2}]$, appearing in Eq. (9) through $\tilde{\tau}_{\text{si}}$. Note that because of the degeneracy between G_{eff} & ξ_{si} and N_{si} & ξ_{si} , when comparing models with different N_{si} , the G_{eff} should be scaled according to [35]

$$\tilde{G}_{\text{eff}} = G_{\text{eff}} \left(\frac{T_{\text{si}}}{T_{\text{fs}}} \right)^{5/2} . \quad (14)$$

To test the importance of SI_{dr}, we investigate different scenarios as summarized in Table 2. In cases with non-zero \tilde{N}_{si} , we always allow G to vary freely. The motivation and physical interpolation is clear: case A tests whether SI_{dr} only can account for all the observations; compared with case D where we fix the overall radiations $N_{\text{eff}} = 3.044$ and only vary the interacting strength G , we can test the importance of self-interaction and extra-radiation in solving the H_0 tension. Case B tests which are the data required, SI_{dr} or FS_{dr}; assisted by case C, we then get a better understanding of the roles of G and N_{eff} . In our analysis, we assume massless radiations since the impact of SI_{dr}'s mass is considered negligible, as validated by the study in Ref [35].

Table 2 The different scenarios in this work. A number means the parameter is fixed, and 'free' means the parameter can vary.

	A	B	C	D
N_{fs}	0	free	free	0
N_{si}	free	free	0	3.044

For our analysis, we employ the Markov Chain Monte Carlo (MCMC) method, using the publicly available code **Cobaya** [49] and **Montepython** [50, 51]. We sample from the posterior distributions using the Metropolis-Hastings algorithm implemented in **Cobaya**, and we adopt the Gelman-Rubin convergence criterion [52].

4.1 Data

In our analysis, we make use of the following datasets:

- **Planck**: We utilize the full temperature and temperature-polarization power spectra measured by the Planck collaboration. The likelihood includes low ℓ -TT from **Commander**, $2 \leq \ell \leq 29$; low ℓ -EE from **Simall**, $2 \leq \ell \leq 29$; high ℓ -TT from **PlikHM**, $30 \leq \ell \leq 2508$; high ℓ -TTTEEE from **PlikHM**, $30 \leq \ell \leq 1996$. Further details regarding these likelihoods can be found in [53].
- **CMB Lensing**: We consider the Planck reconstructed CMB lensing power spectrum [53]. The CMB lensing power spectrum probes structures over a broad range of redshift, with a peak at $z \approx 1 - 2$. The scale cuts used in the Planck lensing power spectrum likelihood include modes with $8 \leq L \leq 400$, for which non-linear corrections are negligible.
- **Riess2018a**: We include the local measurement of the Hubble constant by the Hubble Space Telescope, $H_0 = 73.48 \pm 1.66$ [54].
- **Pantheon**: Additionally, we incorporate the Pantheon dataset, which is a compilation of Type Ia supernovae measurements [55].
- **BAO**: We also include measurements of the BAO from the 6dF Galaxy Survey [56], SDSS MGS [57], and SDSS DR12 [58].

Our baseline parameter space consists of nine parameters: the self-interacting strength G_{eff} , the temperature ratio of the dark radiations ξ_{si} , the Hubble constant H_0 , the physical energy density for cold dark matter and baryons $\Omega_c h^2$ and $\Omega_b h^2$ respectively, the reionization optical depth τ_{reio} , the spectrum amplitude A_s , and the spectrum index n_s . Since BBN is affected by N_{eff} , we take Y_p as another free parameter for possible $N_{\text{eff}} \gg 3$. We use the priors suggested by Cobaya⁴. The priors for SIdr are $\xi_{\text{si}} \sim \mathcal{N}(0.7, 0.001)$, $\log_{10}[G_{\text{eff}}/\text{MeV}^{-2}] \sim \mathcal{N}(-1, 0.1)$. These selections are under the following considerations: SIdr is likely to share the same temperature with neutrinos, e.g. sterile neutrino, and a large self-interacting strength is supported by previous studies.

⁴https://cobaya.readthedocs.io/en/latest/cosmo_basic_runs.html

4.2 Results

Our analysis explores two distinct interacting models depending upon their coupling strength: the strong-interacting model with $\log_{10}[G_{\text{eff}}/\text{MeV}^{-2}] > -2.5$ and the medium-interacting model with $\log_{10}[G_{\text{eff}}/\text{MeV}^{-2}] < -2.5$. The impact of these models on various cosmological parameters can be observed in Fig 5, Fig 6 and Fig 7. Due to the parameter degeneracy present in the formation of the power spectrum, the value of $\log_{10}[G_{\text{eff}}/\text{MeV}^{-2}]$ and \tilde{N}_{si} affect parameters such as H_0 , A_s , n_s , τ , Ω_m , and N_{eff} .

One can expect a direct effect that, for the models with only SIDrs, the phase shift in Eq. (10) is cancelled. To keep the observations unchanged, a larger H_0 is required. On smaller scales, this shift is enhanced by the spectral index n_s . Additionally, the SIDr induces an amplification of the amplitude, resulting in a smaller spectrum amplitude A_s .

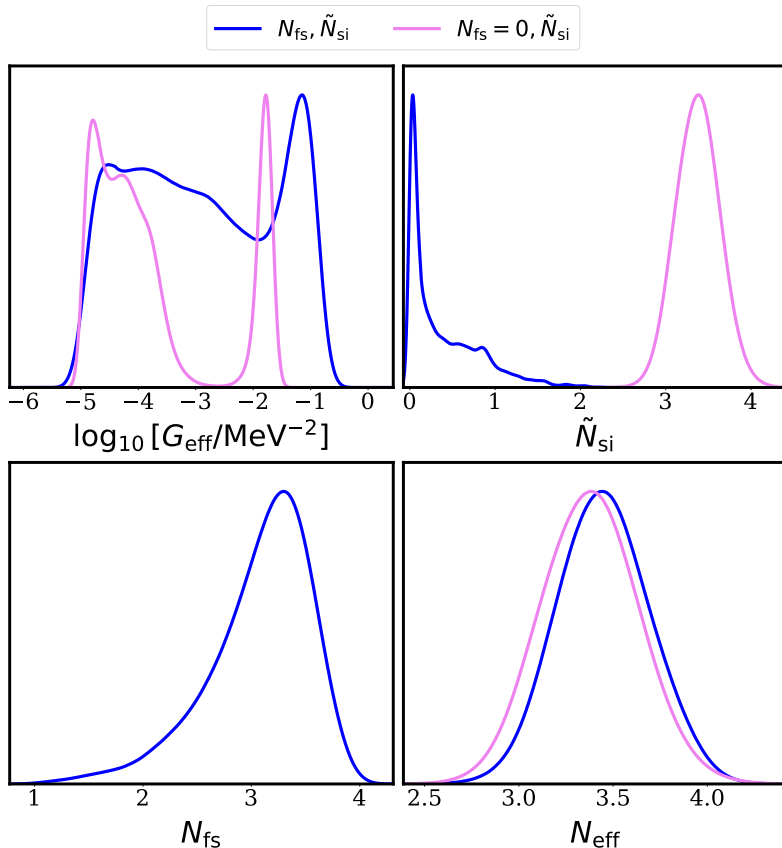


Fig. 5 One-dimensional posterior distribution for $\log_{10}[G_{\text{eff}}/\text{MeV}^{-2}]$, \tilde{N}_{si} , N_{fs} and N_{eff} are presented. The two scenarios are labelled by the parameters $N_{\text{fs}}, \tilde{N}_{\text{si}}$, either fixed or free: SIDr with FSdr (blue) and SIDr only (violet). The violet curves favour the strong coupling and medium coupling between SIDr, as shown in the upper-left panel, while the inclusion of FSdr alters this preference, as indicated in the upper-right panel. Both scenarios exhibit similar predictions for the overall radiation component, as demonstrated in the lower-right panel.

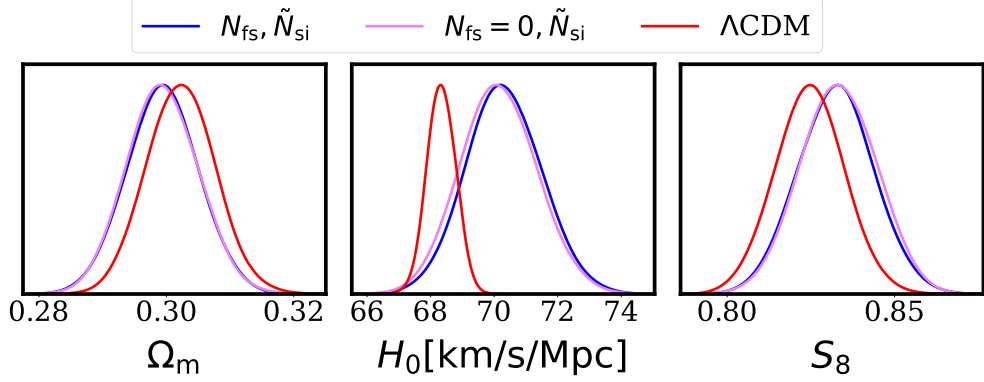


Fig. 6 Similar to Fig. 5, but now considering the parameters Ω_m , H_0 , and S_8 , and incorporating the Λ CDM results. Notably, the Hubble parameter in these two scenarios is increased, alleviating the tension with local measurements, while the tension in S_8 is slightly enhanced. These changes result from the inclusion of SH0ES data and the consideration of N_{eff} as a freely derived parameter.

Fig 5 demonstrates that if SI_{dr} consists of all the dark radiation (the violet curve), there will be a strong coupling region, highly preferred over medium coupling. While when possible FS_{dr} exists, the SI_{dr} components are decreased to around zero and couldn't distinguish strong or medium coupling. When we focus on $\dot{\tau}_{\text{si}}$ for both cases, we find a consistent value due to the degeneracy between interacting strength and temperature, i.e., $\dot{\tau}_{\text{si}} \propto G_{\text{eff}}^2 T_{\text{si}}^5$.

In the subsequent panels of Fig 5, it becomes evident that FS_{dr} plays a vital role, constituting the majority of the dark radiations with a value of $R_{\text{fs}} \approx 0.392$, or equivalently $N_{\text{fs}} = 3.08$. Considering N_{fs} as a free parameter with a uniform prior strongly favors their existence over SI_{dr}, $\tilde{N}_{\text{si}} = 0.37$. Furthermore, we observe that in either case, the overall radiation species number is similar $N_{\text{eff}} \approx 3.45$. This leads to a higher and consistent $H_0 \approx 70.2 \text{ km/s/Mpc}$ estimation in both cases in Fig 6, although the underlying mechanisms differ significantly. One is that the SI_{dr} leads to an increase of H_0 , but additional radiation is required to fix the amplitude and phase in high multipoles. On the other hand, when FS_{dr} are considered, because of the prior from local H_0 measurement, the N_{eff} should be increased. Therefore, once $N_{\text{eff}} > 3.044$ is not allowed, SI_{dr} is inadequate for resolving the Hubble tension, though the tension for now is reduced to 1.39σ . More importantly, a similar outcome is achieved by allowing additional FS_{dr}; thus, the SI_{dr} scenario thus has no advantage.

In Fig 6, both models predict the same value of S_8 , supporting the existence of tension in S_8 . Notably, the best-fit value of S_8 is higher than what is predicted by Λ CDM, a common issue encountered by solutions to reduce the sound horizon.

The Fig 7 illustrates the contour plots for different parameters. We observe that n_s and A_s are the parameters mostly affected by G_{eff} , while other parameters do not show obvious separated regions as expected in the earlier paragraph. The significance of the strong interaction is smaller compared to the medium interaction concerning A_s and n_s . Most parameters are consistent with Λ CDM predictions, except for the

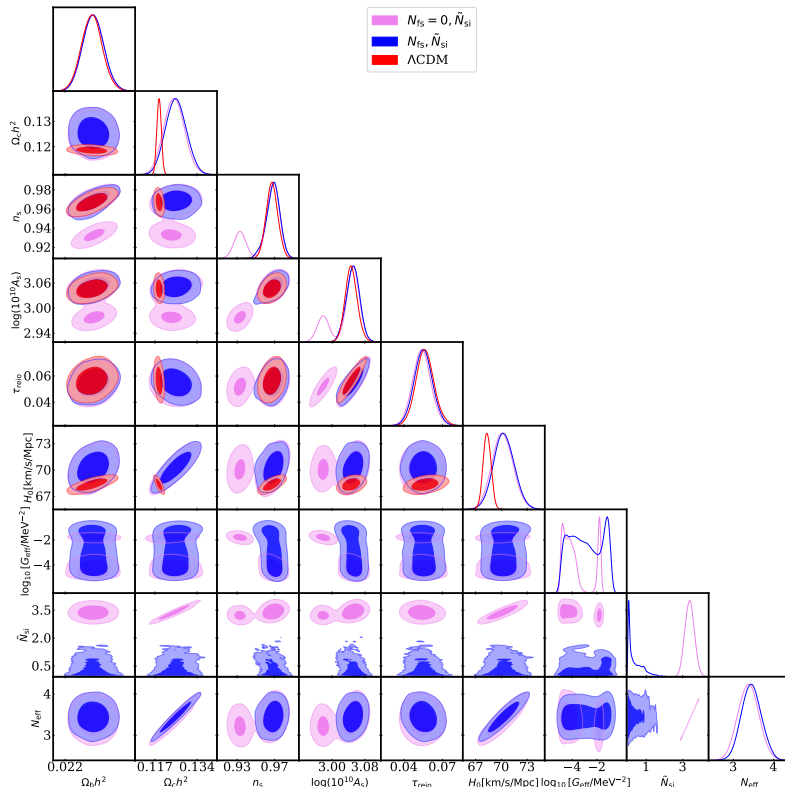


Fig. 7 One-dimensional and two-dimensional posterior distributions for the full cosmological parameter space with $1-\sigma$ and $2-\sigma$ intervals are represented by dark and light-shaded contours, respectively.

physical abundance of dark matter $\Omega_c h^2$, which determines the equality epoch. The rise in ω_c is attributed to the increase in N_{eff} as discussed in [59]:

$$\Delta\omega_c \approx \omega_c^{\Lambda\text{CDM}} \frac{1 + \frac{7}{8} \left(\frac{4}{11}\right)^{4/3} \Delta N_{\text{eff}}}{1 + \frac{7}{8} \left(\frac{4}{11}\right)^{4/3} N_{\text{eff}}^{\Lambda\text{CDM}}} , \quad (15)$$

where Δ gives the difference compared to the value in ΛCDM .

Because most of the information of τ_{reio} comes from large-scale data, the parameter τ_{reio} remains unaffected by the existence of SI_{dr}. Large-scale perturbations enter the horizon at a late time when the nature of the dark radiation doesn't matter⁵.

In Fig 8, we delve into the details of strong and medium self-interactions. The results suggest that the parameter N_{fs} aligns with the ΛCDM in both cases. This implies the presence of FS_{dr} necessary to account for the phase shift in the power spectra. It also indicates a strong tendency toward ΛCDM , allowing for a fraction of SI_{dr} approaching zero, i.e., $\tilde{N}_{\text{si}} = 0.31_{-0.35}^{+0.12}$,

⁵At the late time, the self-scattering rate is far smaller than the universe expansion rate, and thus can be taken as free-streaming radiation.

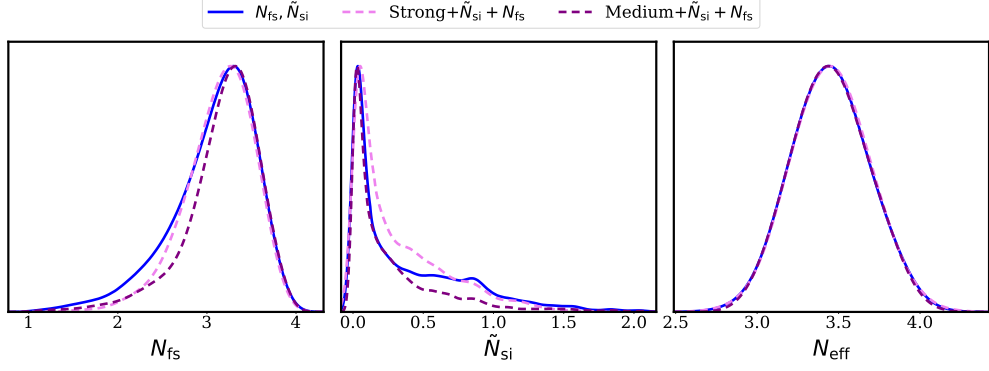


Fig. 8 Same as Fig 6 but for $\tilde{N}_{\text{si}}, N_{\text{fs}}$ and N_{eff} , we split into strong coupling (violet-dashed curve) and medium coupling (purple-dashed curve). In either case, the existence of SI_{dr} is limited compared with FS_{dr}.

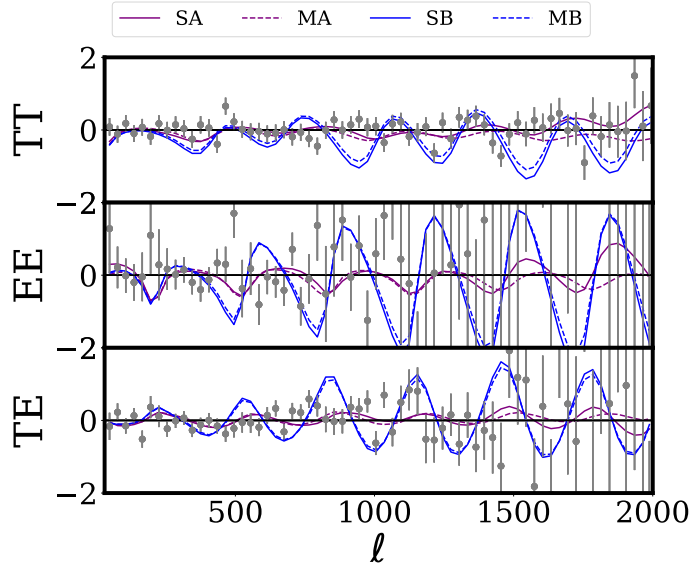


Fig. 9 The fractional difference in TT, EE, TE power spectra in terms of cosmic variance. We show the best-fit results for both strong (solid curves) and medium interacting (dashed curves) regions. The gray error bars show Planck 2018 measurements. The labels are the same as Table 3.

We compare the best-fit power spectrum with that of Λ CDM in terms of the cosmic variance. The oscillations observed in Fig 9 indicate a phase shift compared to the best-fit power spectrum of the Λ CDM. The cosmic variance can be calculated using

the power spectrum C_ℓ :

$$\sigma_{\text{CV}} = \begin{cases} \sqrt{\frac{2}{2\ell+1}} C_\ell^{\text{TT}} & TT ; \\ \sqrt{\frac{2}{2\ell+1}} C_\ell^{\text{EE}} & EE ; \\ \sqrt{\frac{1}{2\ell+1}} \sqrt{C_\ell^{\text{TT}} C_\ell^{\text{EE}} + (C_\ell^{\text{TE}})^2} & TE . \end{cases} \quad (16)$$

As depicted in Fig 9, the model without FSdr remains consistent with the best-fit power spectrum from the Planck data. The differences between the models are not apparent until the deep damping tail for $\ell > 2000$. Therefore, high-resolution experiments will be crucial in distinguishing between these two models. On the other hand, when FSdr are included, the peaks exhibit more out-of-phase oscillations as shown in Fig 9 because of the different N_{eff} from ΛCDM . Additionally, in the second panel, we observe that the E-polarization data from Planck provides limited constraints on the models, especially in the case including FSdr. In Appendix A, we show the result when including ACP and SPT polarization data.

Table 3 The difference in χ^2 between the ΛCDM model is calculated. In this context, "S" represents "Strong" and "M" represents "Medium", indicating the interacting strength. "A" and "B" refer to the scenarios outlined in Table 1. For example, "SA" denotes the strong interacting region for the SI_{dr} only case ($N_{\text{fs}} = 0, \tilde{N}_{\text{si}}$).

Parameter68%	ΛCDM	SA	MA	A	SB	MB	B
$\Delta\chi_{\text{Planck}}^2$	-	6.3	4.0	4.2	3.4	3.6	3.2
$\Delta\chi_{\text{base}}^2$	-	2.6	-1.0	-0.5	-1.9	-1.6	-2.1

We have summarized the statistics in Table 3. The χ^2 values have been calculated compared to the ΛCDM model using the baseline dataset. Here we note the χ^2 in CMB data as χ_{Planck}^2 . Specifically, we test the strong and medium interacting regions in cases A and B. In case A, neither the strong nor medium interacting regions provide a better fit for the CMB data. However, in the baseline dataset, we observe improvement, with medium interaction being more optimal than strong interaction. A similar pattern is seen in case B, which shows a better fit due to adding a new free parameter. The small $\Delta\chi$ between strong and medium interaction indicates the limited influence of SI_{dr}. When comparing cases A and B, we find that a better fit is achieved when FSdr are included, following the trend "strong interaction < medium interaction < no interaction". These results suggest the limited significance of SI_{dr}, at least within the Planck observations.

4.3 What CMB and SH0ES Data Respectively Tell Us

In the previous section, our baseline dataset included both high-redshift and low-redshift data, and we found no evidence for SI_{dr}. However, the conflicting predictions

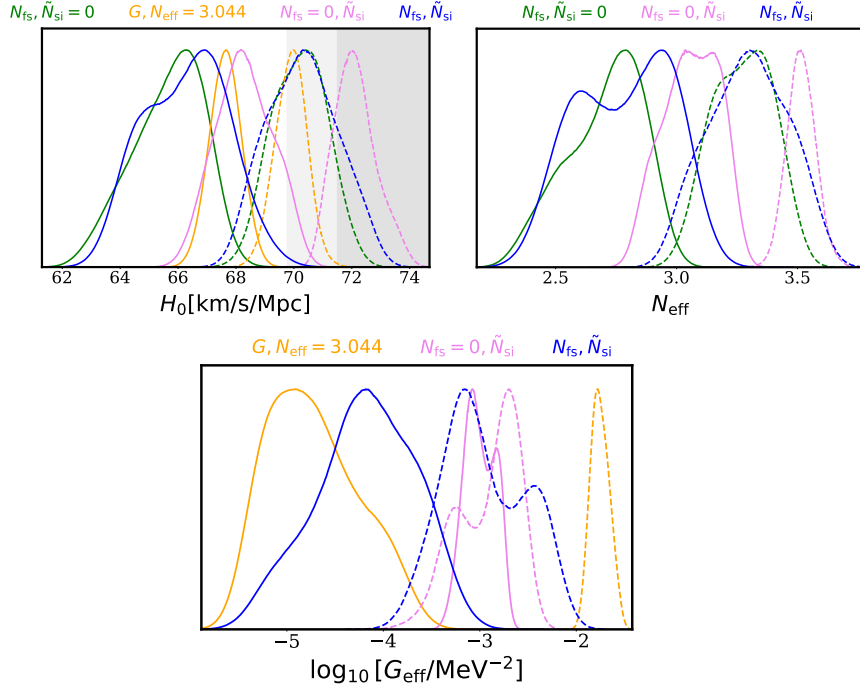


Fig. 10 The one-dimensional posteriors for H_0 , N_{eff} , and $\log_{10}[G_{\text{eff}}/\text{MeV}^{-2}]$ are presented. The solid curves depict predictions based on Planck data, whereas the dashed curves incorporate the SH0ES measurements. The grey-shaded region represents the 2σ confidence interval permitted by SH0ES. The violet, blue, green, and orange curves correspond to scenarios A, B, C, and D, respectively, as detailed in Table 1.

for H_0 from SH0ES and CMB data prevent drawing definitive conclusions by just using the baseline dataset. In this subsection, we analyze models with and without the SH0ES results. Our primary focus is on the CMB data from Planck2018, covering temperature, E-mode polarization, and lensing, as well as the H_0 prior from SH0ES. Details are provided in Section 4.1. As shown in Figure 10, we evaluate four scenarios using only Planck data (solid curves) and Planck combined with SH0ES (dashed curves).

Starting with the solid green curves, this represents the N_{eff} extension to ΛCDM , which yields a low value of H_0 . When local data is included, the dashed green curve shows $H_0 \sim 70$ and an increase in N_{eff} . The solid orange curve predicts a weak interacting strength and a low H_0 value, indicating that the CMB data alone does not favour SI ν r if we fix the radiation species. However, with the inclusion of local data (dashed orange curve), the interacting strength becomes significant, leading to a higher H_0 value. This behaviour shows the virtue of the SI ν r model, reducing the tension to 1.8σ . However, from the orange solid and dashed curves, we see the trouble of SI ν r that CMB data doesn't automatically prefer.

The most surprising result comes from the pink curves. The solid pink curve shows $N_{\text{eff}} \sim 3$ while reducing the H_0 tension to 2.4σ . This reduction in tension is a combined

result of the self-interacting nature of SI_{dr} and the increased error in N_{eff} . However, including local data does not shift the interacting strength, as shown by the overlapping pink dashed and solid curves in the third panel. We still observe a higher H_0 value, consistent with the increase in N_{eff} , supporting our previous analysis that SI_{dr} alone does not resolve the tension.

Finally, the blue solid curves in H_0 and N_{eff} closely follow the green ones but with minor features similar to the violet curves, indicating that FS_{dr} dominates over SI_{dr}, further supporting our conclusions.

In conclusion, without a prior on H_0 , the CMB data does not necessitate SI_{dr} to be self-interacting. However, moderate interacting strength helps to reduce the tension to 3σ . When SH0ES data is included, the FS_{dr} model is preferred over the SI_{dr} model.

5 Fisher Forecast

We have observed the significance of polarization data in constraining the properties of dark radiations. Thus, it becomes crucial to achieve a more precise detection of the CMB sky map, which improves the determination of peak amplitudes and phases and reduces the marginalised error. These advancements will greatly enhance our ability to constrain dark physics. In this section, we employ the Fisher forecast method to assess the potential of upcoming CMB experiments in constraining dark physics.

The Fisher matrix formalism is a widely used tool for predicting the statistical capabilities of future experiments in measuring cosmological parameters. It is defined as the expectation value of the second derivative matrix of the logarithm of the likelihood function with respect to the parameters of interest:

$$F_{ij} = - \left\langle \frac{\partial^2 \ln L}{\partial \theta_i \partial \theta_j} \right\rangle, \quad (17)$$

where the average is taken over all possible realizations of the data assuming a certain fiducial model. The errors in the parameters can be obtained from the inverse of the diagonal Fisher information matrix:

$$\sigma(\theta_i) = (F^{-1})_{ii}^{1/2}. \quad (18)$$

The Cramér-Rao bound states that the errors obtained from the Fisher information matrix represent the smallest achievable errors for unbiased estimators. In the case of a Gaussian likelihood, the components of the Fisher matrix are given by [60]:

$$F_{ij} \equiv \sum_{\ell} F_{\ell}^{ij} = \sum_{\ell} \frac{2\ell + 1}{2} f_{\text{sky}} \text{Tr} \left(\mathbf{C}_{\ell}^{-1}(\vec{\theta}) \frac{\partial \mathbf{C}_{\ell}}{\partial \theta_i} \mathbf{C}_{\ell}^{-1}(\vec{\theta}) \frac{\partial \mathbf{C}_{\ell}}{\partial \theta_j} \right). \quad (19)$$

where we have defined the Fisher information for single ℓ -component F_ℓ^{ij} and f_{sky} is the sky coverage. \mathbf{C}_ℓ is a matrix that containing various observables:

$$\mathbf{C}_\ell \equiv \begin{pmatrix} C_\ell^{TT} + N_\ell^{TT} & C_\ell^{TE} & C_\ell^{T\phi} & 0 \\ C_\ell^{TE} & C_\ell^{EE} + N_\ell^{EE} & 0 & 0 \\ C_\ell^{T\phi} & 0 & C_\ell^{\phi\phi} + N_\ell^{\phi\phi} & 0 \\ 0 & 0 & 0 & C_\ell^{BB} + N_\ell^{BB} \end{pmatrix}. \quad (20)$$

In this section, ϕ is the lensing potential [61]. We extend Eq. (20) by including the B-mode power spectrum. We assume a white-noise power spectrum $N_\ell^{XX'}$ for the effective noise, where $XX' \in \{TT, EE, TE, BB\}$, is given by;

$$N_\ell^{XX'} = s^2 \exp\left(\ell(\ell+1) \frac{\theta_{\text{FWHM}}^2}{8 \log 2}\right), \quad (21)$$

where θ_{FWHM} represents the experimental resolution, s is the instrumental noise in temperature, and $\sqrt{2}s$ is the noise in polarization. The noise for lensing potential is reconstructed according to [61]. The Fisher forecast is performed through a modification of the public code **Fishchips** [62].

In this study, we compare three categories of experiments: the current state-of-the-art CMB data provided by the Planck satellite, and the improved large-scale polarization CMB measurements from the scheduled experiment in Tibet⁶; the Stage-4 CMB experiment (CMB-S4) [76]. Details of the experimental configurations we use is summarized in Table 4.

Table 4 The experimental parameters used for the fisher analyses.

Experiment	ℓ -range	Noise s [$\mu\text{K-arcmin}$]	f_{sky}	θ_{FWHM} [arcmin]
Planck	2-2500	43	0.6	5
AliCPT	20-1000	8.6	0.1~0.4	11.0
CMB-S4	300-3000	1.0	0.4	1.5

We assume equal ℓ -band coverage across different channels, including temperature, polarization-E, and lensing potential. The fiducial cosmology model we used is based on the best-fit parameters in Section 4.2 for the model $N_{\text{fs}}, \tilde{N}_{\text{si}}$ in the strong self-interacting region. The parameters we're interested in this section are those related to dark radiations, so we vary the following parameter set $\{\log_{10}[G_{\text{eff}}/\text{MeV}^{-2}], \tilde{N}_{\text{si}}, N_{\text{fs}}, H_0\}$. Furthermore, we conducted an analysis to evaluate the potential improvement achieved by incorporating polarization B-mode data. However, our findings indicate that, even in CMB-S4 experiments, the contribution from polarization B-mode data is consistently limited, as illustrated in Fig 11 and Fig 12.

⁶This is a CMB degree-scale polarimeter to be deployed on the Tibetan plateau, dubbed as the Ali CMB Polarization Telescope (AliCPT) [63–66]. Some related studies of this project can be found in [67–75] and references therein.

5.1 Results

First, we present the Fisher information for the Hubble constant across all ℓ bands defined in Eq. 19, neglecting the covariance between different parameters (see Fig 11).

On larger scales, the AliCPT could provide more information compared to Planck due to its lower noise level, depending on the sky coverage. However, $f_{\text{sky}} < 0.2$ yields less information than Planck data. On smaller scales, the CMB-S4 experiment dominates due to its high resolution. The inclusion of polarization B-mode data does not significantly improve the results on H_0 but contributes at the level of $\mathcal{O}(0.1)$ to the interacting strength $\log_{10}[G_{\text{eff}}/\text{MeV}^{-2}]$ as indicated by the blue curves.

For Planck data, the information is primarily concentrated in the middle bands $300 < \ell < 1800$, beyond which it decreases rapidly. Due to improved noise control in CMB-S4, it provides abundant information in the far damping tail for $\ell > 1800$. We can propose that CMB-S4 alone cannot provide information about large scales. Thus, combining these three experiments will have the best capacity over the entire ℓ band.

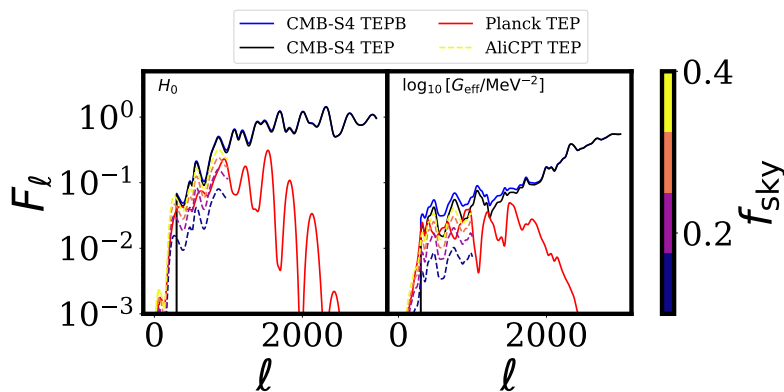


Fig. 11 Fisher information for H_0 and $\log_{10}[G_{\text{eff}}/\text{MeV}^{-2}]$ across ℓ bands considering CMB experiments. For the AliCPT configuration, we varied the sky coverage from 0.1 to 0.4 (dashed lines).

After having constructed the Fisher matrix in Eq.19, we can obtain an expected error covariance matrix on the parameter space by inverting the Fisher matrix.

$$C_{ij} = (F^{-1})_{ij} . \quad (22)$$

We present the result of Eq. 22 in Fig 12 Different configurations have been applied: the CMB-S4 experiment using CMB temperature, polarization E, and lensing potential power spectrum, the same configuration including polarization B power spectrum, a combination of Planck, AliCPT (assuming $f_{\text{sky}} = 0.4$), and CMB-S4 experiments using the entire CMB power spectrum. We use equal bands for different channels according to the corresponding experiment configuration in Table 4. Although including the B power spectrum has limited improvement on a single parameter, it helps decrease the degeneracy between neutrinos and dark radiations.

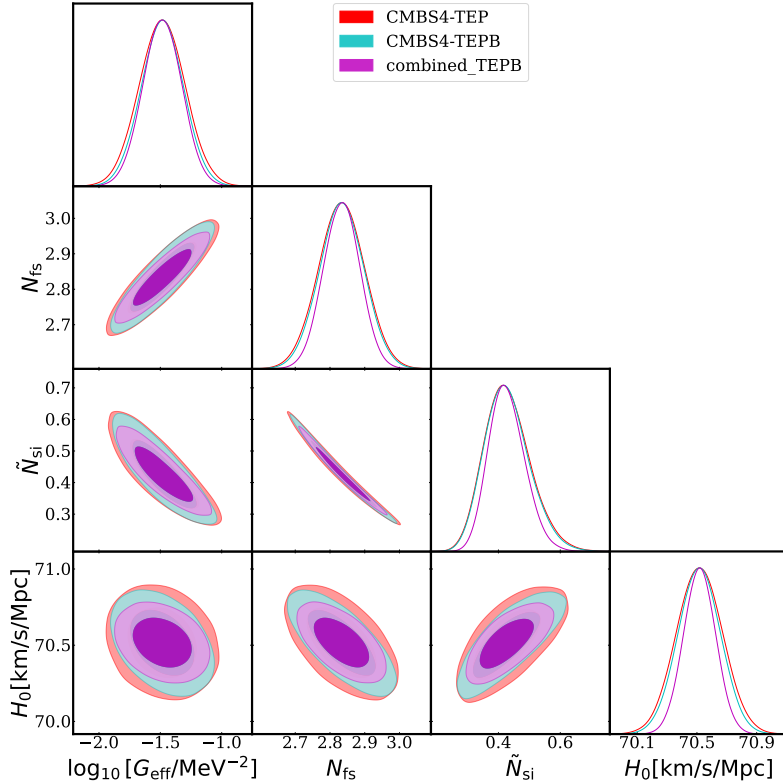


Fig. 12 Posteriors from a simplified Fisher forecast for CMB-S4 like measurements of the CMB temperature, E polarization and lensing information. We have considered the optimal case for the sky coverage in the AliCPT experiment, i.e., $f_{\text{sky}} = 0.4$.

Table 5 The prediction errors of parameters corresponding to different CMB experiments based on Fisher analysis.

Parameter	Planck-TEP	CMB-S4-TEP	CMB-S4-TEPB	combined-TEPB
$\log_{10}[G_{\text{eff}}/\text{MeV}^{-2}]$	0.76	0.18	0.17	0.15
H_0	0.35	0.15	0.14	0.11
N_{fs}	0.18	0.063	0.062	0.051
\tilde{N}_{si}	$(-0.25, 0.12)$	$(-0.078, 0.061)$	$(-0.078, 0.060)$	$(-0.062, 0.050)$

To quantify the capacity for parameter constrain, we calculate the marginalized 1σ error on a single parameter and compare the difference in this error between configurations. We have concluded all the results in Table 5. The detection significance can be easily calculated using z-score $z = (x - \mu)/\sigma$, e.g. $(2.49\sigma, 6.19\sigma, 6.22\sigma, 7.64\sigma)$ for \tilde{N}_{si}

6 Conclusions and Outlook

The existence of Self-Interacting dark radiations can have significant impacts on the universe's evolution. When SIdr enter the sound horizon, it remains coupled, thereby

amplifying the radiation driving effects. Consequently, the phase and amplitude of these scales in the power spectrum are shifted. Therefore, SI_{dr} becomes a possible method for addressing discrepancies between observations.

This study introduces a temperature ratio as a free parameter, denoted as ξ_{si} , between dark radiation and photons. This departs from previous work where the integer flavors of dark radiations were specified [34]. This parameter along with the interacting strength $\log_{10}[G_{\text{eff}}/\text{MeV}^{-2}]$ captures all the properties of SI_{dr}. When neglecting parameter degeneracies, theoretical analysis shows that without explicitly incorporating additional radiation, $N_{\text{eff}} = 3.02 \pm 0.27$, and an increased Hubble constant $H_0 = 69.3 \pm 2.0 \text{ km/s/Mpc}$ naturally emerges when all dark radiations were are tightly coupled. This makes SI_{dr} a hopeful solution to the Hubble tension.

We employed the latest CMB data from the Planck experiment, BAO data from SDSS, supernova (SN) data from Pantheon, and local H_0 measurements from SH0ES to constrain the SI_{dr} model and address the Hubble tension. The results have been further validated using data from the Atacama Cosmology Telescope (ACT) and the South Pole Telescope (SPT).

The predictions for the most cosmological parameters are consistent for all the datasets, and an increased Hubble constant, i.e. approximately $H_0 \approx 70 \text{ km/s/Mpc}$, has been achieved. The SI_{dr} only (scenario A) aligns more closely with Planck results for parameters such as $N_{\text{eff}} = 3.23 \pm 0.25$, although it degrades the fits to both the CMB data and the baseline dataset. Furthermore, a strong interaction result does not fit well compared to a medium interaction, with the limitation being ΛCDM . When considering the inclusion of FS_{dr}, the existence of SI_{dr} is disfavored. Although incorporating SI_{dr} leads to an increase in the Hubble constant, it also increases the effective number of neutrino species (N_{eff}). Considering the results from Fig 5 and Fig 6, which illustrate scenarios A ($N_{\text{fs}} = 0, \tilde{N}_{\text{si}}$) and B ($N_{\text{fs}}, \tilde{N}_{\text{si}}$), we observe that SI_{dr} helps alleviate the tension. However, in the latter case, we get $\tilde{N}_{\text{si}} \sim 0$. This indicates that while SI_{dr} may exist, it cannot dominate over FS_{dr} in addressing the Hubble tension. To further investigate the evidence for SI_{dr}, we compare the four scenarios A, B, C, D (discussed in Sec 4.3) using both Planck data alone and in combination with SH0ES data. Although SI_{dr} can reduce the tension even without an H_0 prior, the inclusion of SH0ES data predicts the same interacting strength for SI_{dr}, thereby diminishing confidence in SI_{dr} as a solution to the tension, as opposed to additional radiation. This concern is further reinforced when considering FS_{dr}. Therefore, no evidence supports the hypothesis that SI_{dr} can resolve the H_0 problem.

As another cross-check, we analyze the SPT and ACT data, which provide more moderate results. These datasets support the existence of approximately 1 flavor SI_{dr} in the radiations component while raising N_{eff} to 3.52. The all-coupling case is consistently disfavored by all the datasets since it degrades the fits. Although ACT-SPT data leaves some room for the existence of SI_{dr}, it doesn't play the role that solves the Hubble tension.

Lastly, we employed a Fisher forecast analysis to predict future constraints on the SI_{dr} model. A 32% measurement on SI_{dr} specie will be obtained using CMB-S4 experiment. When combined with AliCPT and Planck experiments, we will get a 26% measurement.

FSdr leaves another featured observation on Large Scale Structure (LSS), which includes more modes than the 2 dimension CMB map. Thus, researching dark radiations with LSS will give more information. We leave this topic in the near future.

Acknowledgments. The authors thank Pierre Zhang for the fruitful comments. Thanks the pioneering work by Das and Kreisch. Thanks to the public code cobaya, Class and Class_SInu. This work is supported in part by the National Key R&D Program of China (2021YFC2203100), CAS Young Interdisciplinary Innovation Team (JCTD-2022-20), NSFC (12261131497, 11653002), 111 Project for “Observational and Theoretical Research on Dark Matter and Dark Energy” (B23042), Fundamental Research Funds for Central Universities, CSC Innovation Talent Funds, USTC Fellowship for International Cooperation, USTC Research Funds of the Double First-Class Initiative, CAS project for young scientists in basic research (YSBR-006). Kavli IPMU is supported by World Premier International Research Center Initiative (WPI), MEXT, Japan. We acknowledge the use of computing facilities of astronomy department, as well as the clusters LINDA & JUDY of the particle cosmology group at USTC.

Appendix A Other dataset

As the Planck polarization data limits the existence of SIdr, we investigate the possible SIdr in ACT and SPT data. As shown in Fig A1, $\tilde{N}_{\text{si}} \approx 1$ even when FSdr exists.

References

- [1] Riess, A.G., *et al.*: A 2.4% Determination of the Local Value of the Hubble Constant. *Astrophys. J.* **826**(1), 56 (2016) <https://doi.org/10.3847/0004-637X/826/1/56> [arXiv:1604.01424](https://arxiv.org/abs/1604.01424) [astro-ph.CO]
- [2] Ade, P.A.R., *et al.*: Planck 2013 results. XVI. Cosmological parameters. *Astron. Astrophys.* **571**, 16 (2014) <https://doi.org/10.1051/0004-6361/201321591> [arXiv:1303.5076](https://arxiv.org/abs/1303.5076) [astro-ph.CO]
- [3] Bernal, J.L., Verde, L., Riess, A.G.: The trouble with H_0 . *JCAP* **10**, 019 (2016) <https://doi.org/10.1088/1475-7516/2016/10/019> [arXiv:1607.05617](https://arxiv.org/abs/1607.05617) [astro-ph.CO]
- [4] Freedman, W.L.: Cosmology at a Crossroads. *Nature Astron.* **1**, 0121 (2017) <https://doi.org/10.1038/s41550-017-0121> [arXiv:1706.02739](https://arxiv.org/abs/1706.02739) [astro-ph.CO]
- [5] Aghanim, N., *et al.*: Planck 2018 results. VI. Cosmological parameters. *Astron. Astrophys.* **641**, 6 (2020) <https://doi.org/10.1051/0004-6361/201833910> [arXiv:1807.06209](https://arxiv.org/abs/1807.06209) [astro-ph.CO]. [Erratum: *Astron. Astrophys.* 652, C4 (2021)]
- [6] Di Valentino, E., Mena, O., Pan, S., Visinelli, L., Yang, W., Melchiorri, A., Mota, D.F., Riess, A.G., Silk, J.: In the realm of the Hubble tension—a review

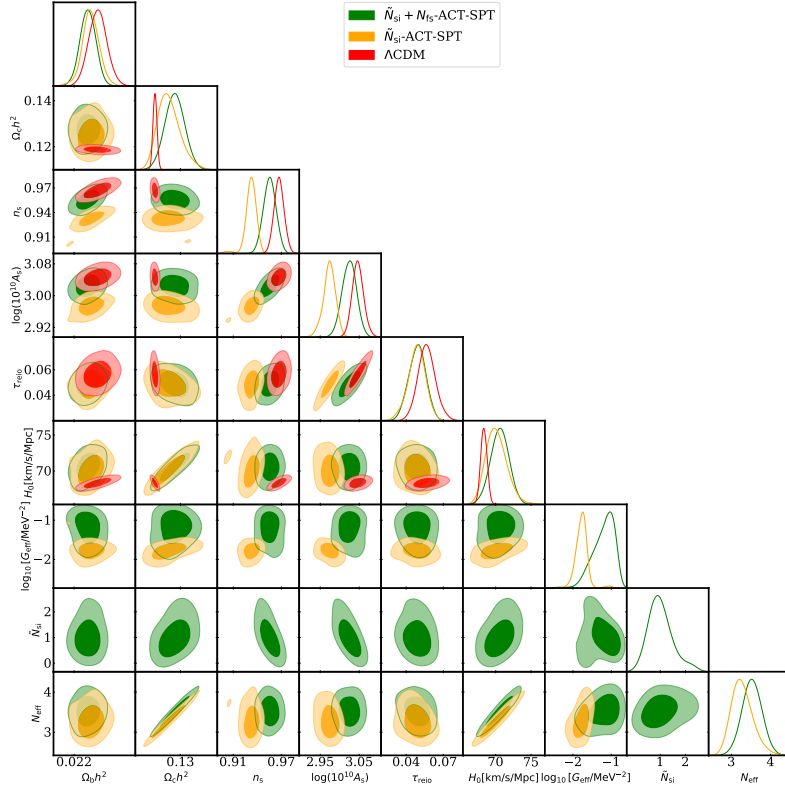


Fig. A1 Same as Fig 7 while green contours correspond to SIdr with neutrinos, yellow are SIdr only. Here we combine Planck, ACT, and SPT for these scenarios. The red contours are Λ CDM use the baseline dataset.

of solutions. *Class. Quant. Grav.* **38**(15), 153001 (2021) <https://doi.org/10.1088/1361-6382/ac086d> [arXiv:2103.01183](https://arxiv.org/abs/2103.01183) [astro-ph.CO]

- [7] Heymans, C., *et al.*: KiDS-1000 Cosmology: Multi-probe weak gravitational lensing and spectroscopic galaxy clustering constraints. *Astron. Astrophys.* **646**, 140 (2021) <https://doi.org/10.1051/0004-6361/202039063> [arXiv:2007.15632](https://arxiv.org/abs/2007.15632) [astro-ph.CO]
- [8] Hill, J.C., McDonough, E., Toomey, M.W., Alexander, S.: Early dark energy does not restore cosmological concordance. *Phys. Rev. D* **102**(4), 043507 (2020) <https://doi.org/10.1103/PhysRevD.102.043507> [arXiv:2003.07355](https://arxiv.org/abs/2003.07355) [astro-ph.CO]
- [9] Ackerman, L., Buckley, M.R., Carroll, S.M., Kamionkowski, M.: Dark Matter and Dark Radiation. *Phys. Rev. D* **79**, 023519 (2009) <https://doi.org/10.1103/PhysRevD.79.023519> [arXiv:0810.5126](https://arxiv.org/abs/0810.5126) [hep-ph]
- [10] Kumar, S., Nunes, R.C., Yadav, S.K.: Cosmological bounds on dark matter-photon coupling. *Phys. Rev. D* **98**(4), 043521 (2018) <https://doi.org/10.1103/PhysRevD.98.043521>

[PhysRevD.98.043521](#) [arXiv:1803.10229](#) [astro-ph.CO]

- [11] Ghosh, S., Khatri, R., Roy, T.S.: Can dark neutrino interactions phase out the Hubble tension? *Phys. Rev. D* **102**(12), 123544 (2020) <https://doi.org/10.1103/PhysRevD.102.123544> [arXiv:1908.09843](#) [hep-ph]
- [12] Schiavone, T., Montani, G., Bombacigno, F.: $f(R)$ gravity in the Jordan frame as a paradigm for the Hubble tension. *Mon. Not. Roy. Astron. Soc.* **522**(1), 72–77 (2023) <https://doi.org/10.1093/mnrasl/slad041> [arXiv:2211.16737](#) [gr-qc]
- [13] Montani, G., De Angelis, M., Bombacigno, F., Carlevaro, N.: Metric $f(R)$ gravity with dynamical dark energy as a paradigm for the Hubble Tension (2023) [arXiv:2306.11101](#) [gr-qc]
- [14] Papanikolaou, T.: The H_0 tension alleviated through ultra-light primordial black holes: an information insight through gravitational waves. In: CORFU2022: 22th Hellenic School and Workshops on Elementary Particle Physics and Gravity (2023)
- [15] Mangano, G., Miele, G., Pastor, S., Pinto, T., Pisanti, O., Serpico, P.D.: Relic neutrino decoupling including flavour oscillations. *Nuclear Physics B* **729**(1-2), 221–234 (2005)
- [16] Bennett, J.J., Buldgen, G., De Salas, P.F., Drewes, M., Gariazzo, S., Pastor, S., Wong, Y.Y.Y.: Towards a precision calculation of N_{eff} in the Standard Model II: Neutrino decoupling in the presence of flavour oscillations and finite-temperature QED. *JCAP* **04**, 073 (2021) <https://doi.org/10.1088/1475-7516/2021/04/073> [arXiv:2012.02726](#) [hep-ph]
- [17] Vagnozzi, S.: New physics in light of the H_0 tension: An alternative view. *Phys. Rev. D* **102**(2), 023518 (2020) <https://doi.org/10.1103/PhysRevD.102.023518> [arXiv:1907.07569](#) [astro-ph.CO]
- [18] Rubakov, V.A., Gorbunov, D.S.: Introduction to the Theory of the Early Universe: Hot Big Bang Theory. World Scientific, Singapore (2017). <https://doi.org/10.1142/10447>
- [19] Kolb, E.W., Turner, M.S.: The Early Universe vol. 69, (1990). <https://doi.org/10.1201/9780429492860>
- [20] Mangano, G., Miele, G., Pastor, S., Pinto, T., Pisanti, O., Serpico, P.D.: Relic neutrino decoupling including flavor oscillations. *Nucl. Phys. B* **729**, 221–234 (2005) <https://doi.org/10.1016/j.nuclphysb.2005.09.041> [arXiv:hep-ph/0506164](#)
- [21] Follin, B., Knox, L., Millea, M., Pan, Z.: First Detection of the Acoustic Oscillation Phase Shift Expected from the Cosmic Neutrino Background. *Phys. Rev. Lett.* **115**(9), 091301 (2015) <https://doi.org/10.1103/PhysRevLett.115.091301>

- [arXiv:1503.07863](#) [astro-ph.CO]
- [22] Baumann, D., Green, D., Wallisch, B.: Searching for light relics with large-scale structure. *JCAP* **08**, 029 (2018) <https://doi.org/10.1088/1475-7516/2018/08/029> [arXiv:1712.08067](#) [astro-ph.CO]
- [23] Baumann, D., Green, D., Zaldarriaga, M.: Phases of New Physics in the BAO Spectrum. *JCAP* **11**, 007 (2017) <https://doi.org/10.1088/1475-7516/2017/11/007> [arXiv:1703.00894](#) [astro-ph.CO]
- [24] Baumann, D.D., Beutler, F., Flauger, R., Green, D.R., Slosar, A., Vargas-Magaña, M., Wallisch, B., Yèche, C.: First constraint on the neutrino-induced phase shift in the spectrum of baryon acoustic oscillations. *Nature Phys.* **15**, 465–469 (2019) <https://doi.org/10.1038/s41567-019-0435-6> [arXiv:1803.10741](#) [astro-ph.CO]
- [25] Escudero, M.: Neutrino decoupling beyond the Standard Model: CMB constraints on the Dark Matter mass with a fast and precise N_{eff} evaluation. *JCAP* **02**, 007 (2019) <https://doi.org/10.1088/1475-7516/2019/02/007> [arXiv:1812.05605](#) [hep-ph]
- [26] Conrad, J.M., Ignarra, C.M., Karagiorgi, G., Shaevitz, M.H., Spitz, J.: Sterile Neutrino Fits to Short Baseline Neutrino Oscillation Measurements. *Adv. High Energy Phys.* **2013**, 163897 (2013) <https://doi.org/10.1155/2013/163897> [arXiv:1207.4765](#) [hep-ex]
- [27] Archidiacono, M., Calabrese, E., Melchiorri, A.: The Case for Dark Radiation. *Phys. Rev. D* **84**, 123008 (2011) <https://doi.org/10.1103/PhysRevD.84.123008> [arXiv:1109.2767](#) [astro-ph.CO]
- [28] Anchordoqui, L.A., Goldberg, H., Steigman, G.: Right-Handed Neutrinos as the Dark Radiation: Status and Forecasts for the LHC. *Phys. Lett. B* **718**, 1162–1165 (2013) <https://doi.org/10.1016/j.physletb.2012.12.019> [arXiv:1211.0186](#) [hep-ph]
- [29] Jacques, T.D., Krauss, L.M., Lunardini, C.: Additional Light Sterile Neutrinos and Cosmology. *Phys. Rev. D* **87**(8), 083515 (2013) <https://doi.org/10.1103/PhysRevD.87.083515> [arXiv:1301.3119](#) [astro-ph.CO]. [Erratum: *Phys.Rev.D* **88**, 109901 (2013)]
- [30] Kreisch, C.D., Cyr-Racine, F.-Y., Doré, O.: Neutrino puzzle: Anomalies, interactions, and cosmological tensions. *Phys. Rev. D* **101**(12), 123505 (2020) <https://doi.org/10.1103/PhysRevD.101.123505> [arXiv:1902.00534](#) [astro-ph.CO]
- [31] Oldengott, I.M., Rampf, C., Wong, Y.Y.Y.: Boltzmann hierarchy for interacting neutrinos I: formalism. *JCAP* **04**, 016 (2015) <https://doi.org/10.1088/1475-7516/2015/04/016> [arXiv:1409.1577](#) [astro-ph.CO]
- [32] D’Eramo, F., Ferreira, R.Z., Notari, A., Bernal, J.L.: Hot Axions and the H_0

- tension. JCAP **11**, 014 (2018) <https://doi.org/10.1088/1475-7516/2018/11/014> [arXiv:1808.07430](https://arxiv.org/abs/1808.07430) [hep-ph]
- [33] Poulin, V., Smith, T.L., Grin, D., Karwal, T., Kamionkowski, M.: Cosmological implications of ultralight axionlike fields. Phys. Rev. D **98**(8), 083525 (2018) <https://doi.org/10.1103/PhysRevD.98.083525> [arXiv:1806.10608](https://arxiv.org/abs/1806.10608) [astro-ph.CO]
- [34] Das, A., Ghosh, S.: Flavor-specific interaction favors strong neutrino self-coupling in the early universe. JCAP **07**, 038 (2021) <https://doi.org/10.1088/1475-7516/2021/07/038> [arXiv:2011.12315](https://arxiv.org/abs/2011.12315) [astro-ph.CO]
- [35] Das, A., Ghosh, S.: The magnificent ACT of flavor-specific neutrino self-interaction (2023) [arXiv:2303.08843](https://arxiv.org/abs/2303.08843) [astro-ph.CO]
- [36] Archidiacono, M., Hannestad, S., Hansen, R.S., Tram, T.: Cosmology with self-interacting sterile neutrinos and dark matter - A pseudoscalar model. Phys. Rev. D **91**(6), 065021 (2015) <https://doi.org/10.1103/PhysRevD.91.065021> [arXiv:1404.5915](https://arxiv.org/abs/1404.5915) [astro-ph.CO]
- [37] Zaldarriaga, M., Harari, D.D.: Analytic approach to the polarization of the cosmic microwave background in flat and open universes. Phys. Rev. D **52**, 3276–3287 (1995) <https://doi.org/10.1103/PhysRevD.52.3276> [arXiv:astro-ph/9504085](https://arxiv.org/abs/astro-ph/9504085)
- [38] Bashinsky, S., Seljak, U.: Neutrino perturbations in CMB anisotropy and matter clustering. Phys. Rev. D **69**, 083002 (2004) <https://doi.org/10.1103/PhysRevD.69.083002> [arXiv:astro-ph/0310198](https://arxiv.org/abs/astro-ph/0310198)
- [39] Baumann, D., Green, D., Meyers, J., Wallisch, B.: Phases of New Physics in the CMB. JCAP **01**, 007 (2016) <https://doi.org/10.1088/1475-7516/2016/01/007> [arXiv:1508.06342](https://arxiv.org/abs/1508.06342) [astro-ph.CO]
- [40] Bashinsky, S., Seljak, U.c.v.: Signatures of relativistic neutrinos in cmb anisotropy and matter clustering. Phys. Rev. D **69**, 083002 (2004) <https://doi.org/10.1103/PhysRevD.69.083002>
- [41] Choi, G., Chiang, C.-T., LoVerde, M.: Probing Decoupling in Dark Sectors with the Cosmic Microwave Background. JCAP **06**, 044 (2018) <https://doi.org/10.1088/1475-7516/2018/06/044> [arXiv:1804.10180](https://arxiv.org/abs/1804.10180) [astro-ph.CO]
- [42] Nollett, K.M., Steigman, G.: BBN And The CMB Constrain Light, Electromagnetically Coupled WIMPs. Phys. Rev. D **89**(8), 083508 (2014) <https://doi.org/10.1103/PhysRevD.89.083508> [arXiv:1312.5725](https://arxiv.org/abs/1312.5725) [astro-ph.CO]
- [43] Hu, W., Sugiyama, N.: Anisotropies in the cosmic microwave background: An Analytic approach. Astrophys. J. **444**, 489–506 (1995) <https://doi.org/10.1086/175624> [arXiv:astro-ph/9407093](https://arxiv.org/abs/astro-ph/9407093)

- [44] Lin, M.-X., Raveri, M., Hu, W.: Phenomenology of Modified Gravity at Recombination. *Phys. Rev. D* **99**(4), 043514 (2019) <https://doi.org/10.1103/PhysRevD.99.043514> [arXiv:1810.02333](https://arxiv.org/abs/1810.02333) [astro-ph.CO]
- [45] Cyr-Racine, F.-Y., Sigurdson, K.: Limits on Neutrino-Neutrino Scattering in the Early Universe. *Phys. Rev. D* **90**(12), 123533 (2014) <https://doi.org/10.1103/PhysRevD.90.123533> [arXiv:1306.1536](https://arxiv.org/abs/1306.1536) [astro-ph.CO]
- [46] Ma, C.-P., Bertschinger, E.: Cosmological perturbation theory in the synchronous and conformal Newtonian gauges. *Astrophys. J.* **455**, 7–25 (1995) <https://doi.org/10.1086/176550> [arXiv:astro-ph/9506072](https://arxiv.org/abs/astro-ph/9506072)
- [47] Oldengott, I.M., Tram, T., Rampf, C., Wong, Y.Y.Y.: Interacting neutrinos in cosmology: exact description and constraints. *JCAP* **11**, 027 (2017) <https://doi.org/10.1088/1475-7516/2017/11/027> [arXiv:1706.02123](https://arxiv.org/abs/1706.02123) [astro-ph.CO]
- [48] Blas, D., Lesgourgues, J., Tram, T.: The Cosmic Linear Anisotropy Solving System (CLASS) II: Approximation schemes. *JCAP* **07**, 034 (2011) <https://doi.org/10.1088/1475-7516/2011/07/034> [arXiv:1104.2933](https://arxiv.org/abs/1104.2933) [astro-ph.CO]
- [49] Torrado, J., Lewis, A.: Cobaya: Code for Bayesian Analysis of hierarchical physical models. *JCAP* **05**, 057 (2021) <https://doi.org/10.1088/1475-7516/2021/05/057> [arXiv:2005.05290](https://arxiv.org/abs/2005.05290) [astro-ph.IM]
- [50] Brinckmann, T., Lesgourgues, J.: MontePython 3: boosted MCMC sampler and other features (2018) [arXiv:1804.07261](https://arxiv.org/abs/1804.07261) [astro-ph.CO]
- [51] Audren, B., Lesgourgues, J., Benabed, K., Prunet, S.: Conservative Constraints on Early Cosmology: an illustration of the Monte Python cosmological parameter inference code. *JCAP* **1302**, 001 (2013) <https://doi.org/10.1088/1475-7516/2013/02/001> [arXiv:1210.7183](https://arxiv.org/abs/1210.7183) [astro-ph.CO]
- [52] Gelman, A., Rubin, D.B.: Inference from Iterative Simulation Using Multiple Sequences. *Statist. Sci.* **7**, 457–472 (1992) <https://doi.org/10.1214/ss/1177011136>
- [53] Aghanim, N., *et al.*: Planck 2018 results. V. CMB power spectra and likelihoods. *Astron. Astrophys.* **641**, 5 (2020) <https://doi.org/10.1051/0004-6361/201936386> [arXiv:1907.12875](https://arxiv.org/abs/1907.12875) [astro-ph.CO]
- [54] Riess, A.G., *et al.*: New Parallaxes of Galactic Cepheids from Spatially Scanning the Hubble Space Telescope: Implications for the Hubble Constant. *Astrophys. J.* **855**(2), 136 (2018) <https://doi.org/10.3847/1538-4357/aaadb7> [arXiv:1801.01120](https://arxiv.org/abs/1801.01120) [astro-ph.SR]
- [55] Scolnic, D.M., *et al.*: The Complete Light-curve Sample of Spectroscopically Confirmed SNe Ia from Pan-STARRS1 and Cosmological Constraints from the

- Combined Pantheon Sample. *Astrophys. J.* **859**(2), 101 (2018) <https://doi.org/10.3847/1538-4357/aab9bb> arXiv:1710.00845 [astro-ph.CO]
- [56] Beutler, F., Blake, C., Colless, M., Jones, D.H., Staveley-Smith, L., Campbell, L., Parker, Q., Saunders, W., Watson, F.: The 6dF Galaxy Survey: Baryon Acoustic Oscillations and the Local Hubble Constant. *Mon. Not. Roy. Astron. Soc.* **416**, 3017–3032 (2011) <https://doi.org/10.1111/j.1365-2966.2011.19250.x> arXiv:1106.3366 [astro-ph.CO]
- [57] Ross, A.J., Samushia, L., Howlett, C., Percival, W.J., Burden, A., Manera, M.: The clustering of the SDSS DR7 main Galaxy sample – I. A 4 per cent distance measure at $z = 0.15$. *Mon. Not. Roy. Astron. Soc.* **449**(1), 835–847 (2015) <https://doi.org/10.1093/mnras/stv154> arXiv:1409.3242 [astro-ph.CO]
- [58] Alam, S., *et al.*: The clustering of galaxies in the completed SDSS-III Baryon Oscillation Spectroscopic Survey: cosmological analysis of the DR12 galaxy sample. *Mon. Not. Roy. Astron. Soc.* **470**(3), 2617–2652 (2017) <https://doi.org/10.1093/mnras/stx721> arXiv:1607.03155 [astro-ph.CO]
- [59] Dodelson, S.: *Modern Cosmology*. Academic Press, Amsterdam (2003)
- [60] Wu, W.L.K., Errard, J., Dvorkin, C., Kuo, C.L., Lee, A.T., McDonald, P., Slosar, A., Zahn, O.: A guide to designing future ground-based cmb experiments. *The Astrophysical Journal* **788**(2), 138 (2014) <https://doi.org/10.1088/0004-637X/788/2/138> arxiv:1402.4108 [astro-ph, physics:hep-ph]
- [61] Hu, W., Okamoto, T.: Mass reconstruction with cmb polarization. *The Astrophysical Journal* **574**(2), 566–574 (2002) <https://doi.org/10.1086/341110> arxiv:astro-ph/0111606
- [62] Li, Z., Gluscevic, V., Boddy, K.K., Madhavacheril, M.S.: Disentangling Dark Physics with Cosmic Microwave Background Experiments. *Phys. Rev. D* **98**(12), 123524 (2018) <https://doi.org/10.1103/PhysRevD.98.123524> arXiv:1806.10165 [astro-ph.CO]
- [63] Li, Y.-P., Liu, Y., Li, S.-Y., Li, H., Zhang, X.: Tibet’s Ali: A New Window to Detect the CMB Polarization (2017) arXiv:1709.09053 [astro-ph.IM]
- [64] Kuo, C.-L.: Assessments of Ali, Dome A, and Summit Camp for Mm-wave Observations Using MERRA-2 Reanalysis. *Astrophys. J.* **848**(1), 64 (2017) <https://doi.org/10.3847/1538-4357/aa8b74> arXiv:1707.08400 [astro-ph.IM]
- [65] Li, H., Li, S.-Y., Liu, Y., Li, Y.-P., Zhang, X.: Tibet’s window on primordial gravitational waves. *Nature Astron.* **2**(2), 104–106 (2018) <https://doi.org/10.1038/s41550-017-0373-0> arXiv:1802.08455 [astro-ph.IM]
- [66] Salatino, M., *et al.*: The design of the Ali CMB Polarization Telescope receiver.

- Proc. SPIE Int. Soc. Opt. Eng. **11453**, 114532 (2020) <https://doi.org/10.1117/12.2560709> arXiv:2101.09608 [astro-ph.IM]
- [67] Cai, Y.-F., Zhang, X.: Probing the origin of our universe through primordial gravitational waves by Ali CMB project. *Sci. China Phys. Mech. Astron.* **59**(7), 670431 (2016) <https://doi.org/10.1007/s11433-016-0178-x> arXiv:1605.01840 [astro-ph.IM]
- [68] Li, H., *et al.*: Probing Primordial Gravitational Waves: Ali CMB Polarization Telescope. *Natl. Sci. Rev.* **6**(1), 145–154 (2019) <https://doi.org/10.1093/nsr/nwy019> arXiv:1710.03047 [astro-ph.CO]
- [69] Wu, D., Li, H., Ni, S., Li, Z.-W., Liu, C.-Z.: Detecting Primordial Gravitational Waves: a forecast study on optimizing frequency distribution of next generation ground-based CMB telescope. *Eur. Phys. J. C* **80**(2), 139 (2020) <https://doi.org/10.1140/epjc/s10052-020-7652-0>
- [70] Zhang, Z., Liu, Y., Li, S.-Y., Wu, D.-L., Li, H., Li, H.: Efficient ILC analysis on polarization maps after EB leakage correction. *JCAP* **22**, 044 (2020) <https://doi.org/10.1088/1475-7516/2022/07/044> arXiv:2109.12619 [astro-ph.CO]
- [71] Li, J.-R., Li, C., Jiang, J., Cai, Y.-F., Delabrouille, J., Wu, D., Li, H.: CMB polarization analysis on circular scans. *JCAP* **08**, 033 (2021) <https://doi.org/10.1088/1475-7516/2021/08/033> arXiv:2103.00561 [astro-ph.CO]
- [72] Liu, J., *et al.*: Forecasts on CMB lensing observations with AliCPT-1. *Sci. China Phys. Mech. Astron.* **65**(10), 109511 (2022) <https://doi.org/10.1007/s11433-022-1966-4> arXiv:2204.08158 [astro-ph.CO]
- [73] Zhang, D., Li, J.-R., Li, J., Yang, J., Zhang, Y., Cai, Y.-F., Fang, W., Feng, C.: Future Prospects on Constraining Neutrino Cosmology with the Ali CMB Polarization Telescope. *Astrophys. J.* **946**(1), 32 (2023) <https://doi.org/10.3847/1538-4357/acbe45> arXiv:2112.10539 [astro-ph.CO]
- [74] Wu, Y.-W., Li, S., Liu, Y., Zhang, Z., Liu, H., Li, H.: Study on the filters of atmospheric contamination in ground based CMB observation. *JCAP* **04**, 047 (2023) <https://doi.org/10.1088/1475-7516/2023/04/047> arXiv:2210.09711 [astro-ph.CO]
- [75] Han, J., Hu, B., Ghosh, S., Li, S., Dou, J., Delabrouille, J., Jin, J., Li, H., Liu, Y., Remazeilles, M., *et al.*: Forecasts of CMB lensing reconstruction of AliCPT-1 from the foreground cleaned polarization data. *JCAP* **2023**, 063 (2023) <https://doi.org/10.1088/1475-7516/2023/04/063> arXiv:2303.05705 [astro-ph.CO]
- [76] Abazajian, K.N., *et al.*: CMB-S4 Science Book, First Edition (2016) arXiv:1610.02743 [astro-ph.CO]